Three years of measurements of light-absorbing aerosols over coastal Namibia: seasonality, origin, and transport

Paola Formenti[1,$], Stuart John Piketh[2], Andreas Namwoonde[3], Danitza Klopper[2], Roelof Burger[2], Mathieu Cazaunau[1], Anaïs Feron[1], Cécile Gaimoz[1], Stephen Broccardo[2], Nicola Walton[2], Karine Desboeufs[1], Guillaume Siour[1], Matheus Hanghome[3], Samuel Mafwila[3], Edosa Omoregie[3], Wolfgang Junkermann[4], and Willy Maenhaut[5]

[1] LISA, UMR CNRS 7583, Université Paris Est Créteil et Université Paris Diderot, Institut Pierre Simon Laplace, Créteil, France

[2] School of Geo- and Spatial Science, Unit for Environmental Sciences and Management, North-West University, Potchefstroom, South Africa

[3] Sam Nujoma Marine and Coastal Resources Research Centre (SANUMARC), University of Namibia, Sam Nujoma Campus, Henties Bay, Namibia

[4] Karlsruhe Institute of Technology, Institute of Meteorology and Climate Research, IMK-IFU, Garmisch-Partenkirchen, Germany

[5] Ghent University (UGent), Department of Chemistry, Gent, Belgium

[$] corresponding author (paola.formenti@lisa.u-pec.fr)

Abstract

Continuous measurements between July 2012 and December 2015 at the Henties Bay Aerosol Observatory (HBAO; 22°S, 14°05'E), Namibia, show that, during the austral wintertime, transport of light-absorbing black carbon aerosols occurs at low-level into the marine boundary layer. The average of daily concentrations of equivalent black carbon (eBC) over the whole sampling period is 53 (± 55) ng m^{-3}. Peak values above 200 ng m^{-3} and up to 800 ng m^{-3} occur seasonally from May to August, ahead of the dry season peak of biomass burning in southern Africa (August to October). Analysis of three-day air mass back-trajectories show that air masses from the south Atlantic ocean south of Henties Bay are generally cleaner than air having originated over the ocean north of Henties Bay, influenced by the outflow of the major biomass burning plume, and from the continent, where the wildfires occur. Additional episodic peak concentrations, even for oceanic transport, indicate that pollution from distant sources in South Africa and maritime traffic along the Atlantic ship tracks could be important. While we expect the direct radiative effect to be negligible, the indirect effect on the microphysical properties of the stratocumulus clouds and the deposition to the ocean could be significant and deserve further investigation, specifically ahead of the dry season.

1. Introduction

Aerosol particles of natural and anthropogenic origin affect the Earth's climate and modulate the greenhouse effect of long-lived gases (Boucher et al., 2013). The extent of this modulation depends on their nature, in particular on their chemical composition and size distribution determining their interactions with radiation and clouds. Current understanding suggests that atmospheric aerosols increase the global outgoing shortwave radiation, enhancing the atmospheric albedo, thereby counteracting the warming effect of greenhouse gases (Boucher et al., 2013). However, light-absorbing aerosols, such as black carbon (BC) from fossil fuel combustion and biomass burning, can reduce the amount of outgoing radiation at the top of

2

atmosphere (TOA), finally adding to the greenhouse effect (Haywood and Shine, 1995; Jacobson, 2001; Chung and Seinfeld, 2002; Bond and Bergstrom, 2006; Koch and Del Genio, 2010; Bond et al., 2013). The heating radiative effect of black carbon aerosols is either enhanced or suppressed if they are above or below clouds, respectively (Keil and Haywood, 2003; Koch and Del Genio, 2010). The local heating induced by light-absorption below clouds could modify the cloud properties by enhancing the vertical motion and increasing the cloud cover and liquid water content (Koch and Del Genio, 2010). Finally, by entrainment into clouds, BC-containing aerosols could cause the cloud to evaporate and rise (Hansen et al., 1997) and reduce the cloud mean drop size diameters, increase droplet concentrations and henceforth reflectivity (Seinfeld and Pandis, 1997).

These processes are relevant to the western coast of southern Africa, pointed out by the latest Intergovernmental Panel for Climate Change (IPCC) report as a region where future warming and reductions in precipitation should be severe (Maure et al., 2018).

The west coast of southern Africa is characterised by a persistent and extended stratocumulus cloud deck topping a shallow, stable marine boundary layer maintained by the cold sea-surface temperatures of the Benguela Current (Cook et al., 2004; Tyson and Preston-Whyte, 2002), and by high loading of light-absorbing aerosols, mostly from seasonal biomass burning in the austral dry season (Swap et al., 2002), but possibly from various local and distant anthropogenic activities including ship traffic and energy production (Piketh et al., 1999; Formenti et al., 1999; Tournadre, 2004). Stratocumulus clouds are highly reflective and efficient in modifying the net radiative balance at TOA (Boucher et al., 2013). However, the mechanisms by which they could interact with light-absorbing aerosols, and the direct and indirect effects of those interactions on the regional radiative budget are largely unknown (Keil and Haywood, 2003; Flato et al., 2013; Myhre et al., 2013).

70   To address these questions, a large observational effort was initiated in the last few years by a

71   number of coordinated intensive airborne and ground-based field campaigns, analysis of

72   spaceborne observations, and climate modelling (Zuidema et al., 2016). These experiments

73   focused on the dry season period between July and October, when biomass burning aerosols

74   contribute by optically-dense plumes with instantaneous aerosol optical depth (AOD)

75   systematically larger than 0.5 at mid-visible wavelengths (Swap et al., 200é). The emission,

76   transport and direct radiative effect of light-absorbing carbonaceous aerosols by biomass

77   burning aerosols also motivated previous experiments, such as the Southern African Regional

78   Science Initiative (SAFARI 2000, Swap et al., 200é) and the Southern African Fire-Atmosphere

79   Research Initiative (SAFARI, Andreae et al., 1996).

80   However, little is known about the aerosol concentrations and properties outside this season.

81   To fill this gap, this paper present the first results of the mass concentrations of light-absorbing

82   carbonaceous aerosols on the Atlantic coast of Namibia from three years of observations at the

83   Henties Bay Aerosol Observatory (HBAO, 22°S, 14°05'E) long-term ground-based surface

84   station.

85   Measurements of the mass concentrations of equivalent black carbon (eBC) recorded between

86   July 2012 and December 2015 in the marine boundary layer below the stratocumulus deck are

87   analysed to gather new knowledge on importance and seasonality. Observations are coupled

88   with calculations of air mass back-trajectories to identify the dominant transport patterns and

89   quantify their contributions. A comparison to the MERRA-2 model reanalysis is performed.

90   **2. Methods**

91   Surface observations of aerosol particles are conducted at the Henties Bay Aerosol Observatory

92   (HBAO, www.hbao.cnrs.fr), a recent regional station in the Global Atmosphere Watch (GAW)

93   Programme of the World Meteorological Organization (WMO). The research centre is located

94   on the Sam Nujoma Marine and Coastal Resources Research Centre (SANUMARC) of the

95   University of Namibia in Henties Bay (22°S, 14°05'E), Namibia (Figure 1). Henties Bay is a

96   small town in an arid environment with no vegetation, no industrial activity and very little

97   traffic. Energy usage is predominantly a mix of electricity and gas, with some solid fuel

98   combustion (wood) due to low availability (A. Namwoonde, 2017, *pers. comm.*). The

99   monitoring site, situated on the University campus, is located on the coast approximately 100 m

100 from the shore line. To the east are the Namibian Gravel Plains, at 3 km to the south of the

101 campus is the town of Henties Bay, and to the north is the Omaruru Riverbed (river mouth

102 approximately 100 m from SANUMARC). The population of Henties Bay ranges between 4

103 600 and 6 000 inhabitants, according to the Namibia 2011 population and housing census (main

104 report available at http://cms.my.na/assets/documents/p19dmn58guram30ttun89rdrp1.pdf).

105 **2.1. Measurements of light-optical attenuation**

106 Instruments at HBAO operate from a roof terrace at approximately 30 m above the ground. The

107 terrace hosts the sampling inlets, from which air is drawn into a laboratory room located

108 underneath by straight stainless-steel pipes to avoid particle losses. The optical attenuation of

109 light (ATN) by aerosol particles smaller than 1 μm in aerodynamic diameter was measured by

110 a single-wavelength aethalometer (model AE-14U, Magee Sci., Berkeley, CA) operating at 880

111 nm and sampling at 3.5 ($\pm$ 0.1) L min^{-1} from a certified PM_1 inlet (BGI Inc., Waltham, MA).

112 The physical principle of operation of the aethalometer is detailed in Hansen et al. (1984).

113 Measurements were performed at a 5-min time resolution and stored on a data logger (model

114 CR-1000, Campbell Sci. Ltd.). The original data set was screened to eliminate spikes and peaks

115 lasting less than two hours, generally associated with open fires for barbequing meat. The data

116 record extended from July 2012 to December 2015, with an extended data gap between January

117 and July 2014 due instrument maintenance.

118   The Lambert-Beer law relates the temporal variation of the measured light-attenuation (ATN)

119   due to aerosol particles collected on a quartz fibre tape to the mass concentration of eBC (in μg

120   m^{-3}). This is based on the fact that black carbon is the strongest light-absorber in the near

121   infrared (Kirchstetter et al., 2004; Caponi et al., 2017).

122   The operational equation linking eBC to the attenuation (ATN) measured by the aethalometer

123   is

124

125 $$\text{eBC} = \frac{1}{\text{MAC}_{\text{BC}}} \left(\frac{1}{\text{C} \cdot \text{R(ATN)}}\right) \left(\frac{A}{V} \frac{\Delta \text{ATN}}{\Delta t}\right)$$ (1)

126

127   where A represents the area of the aerosol deposit on the filter, V the volumetric flow rate, and

128   ΔATN/Δt is the variation rate of attenuation with time. The terms C and R(ATN) account for

129   measurement artefacts that artificially increase absorption estimated from attenuation

130   measurements. The term C takes into account the multiple scattering effects on the filter due to

131   both the filter fibers and the aerosol particles embedded in it. The factor R(ATN) accounts for

132   the shadowing effect occurring with time as high concentrations of absorbing particles are

133   collected on the filter. Published values of the C parameter at 660 and 880 nm range between

134   1.75 and 6.3 depending on the nature of the light-absorbing aerosols, the measurement

135   environment, and finally on the parametrisation of the corrections (Weingartner et al., 2003;

136   Arnott et al., 2005; Schmid et al., 2006; Collaud-Coen et al., 2010; Segura et al., 2014; Saturno

137   et al., 2017; Di Biagio et al., 2018). These authors show that, regardless of location, values

138   below 3.5 are appropriate for moderately absorbing aerosols whose single scattering albedo

139   (ω$_0$) is above 0.8 at 660 nm. For Mace Head, a coastal site with prevailing marine North Atlantic

140   air masses, Collaud-Coen et al. (2010) reported a mean C value of 3.44 (± 0.21), which we used

141   for HBAO, neglecting any possible wavelength dependence. The parametrisation of the

142 shadowing effect R(ATN) depends on ω_0, henceforth, on the availability of concurrent

143 measurements of the scattering coefficient. This is the case at HBAO, where, however,

144 scattering is measured on the PM_{10} and not on the PM_1 fraction as attenuation is, preventing a

145 meaningful estimate of ω_0. In this case, Collaud-Coen et al. (2010) recommended the

146 Weingartner et al. (2003) correction, leading to a mean value of the R parameter of 0.93, which

147 we assumed for the further analysis.

148 The other crucial parameter in Equation (1) is the mass absorption efficiency of eBC (MAC_{BC},

149 units of $m^2 \ g^{-1}$). Many authors have reported values in the range 5-20 $m^2 \ g^{-1}$ at wavelengths

150 between 550 and 870 nm, and related this variability to the chemical state and age of black

151 carbon aerosols (Liousse et al., 1993; Petzold et al., 1997; Martins et al., 1998; Kirchstetter et

152 al., 2003; Hansen, 2005; Bond and Bergstrom, 2006; Knox et al., 2009; Subramanian et al.,

153 2010; Bond et al., 2013; Zanatta et al., 2016). More recently, Zuidema et al. (2018) reported

154 that the MAC_{BC} at 648 nm at Ascension Island, farther west than HBAO, and at times in its

155 outflow, varied between 14.1 $m^2 \ g^{-1}$ in June to 10.7 $m^2 \ g^{-1}$ in July to October. When

156 extrapolated, these values result in a MAC_{BC} at 870 nm between 7.9 and 10 $m^2 \ g^{-1}$. Their

157 average and standard deviation ($9.0 \pm 1.5 \ m^2 \ g^{-1}$) was retained in our analysis.

158 **2.2. Supporting data**

159 In 2013, the mass concentration of particles of diameter smaller than 2.5 μm in equivalent

160 aerodynamic diameter ($PM_{2.5}$) was sampled by a Tapering Element Oscillating Microbalance

161 (TEOM, model 1400a, Rupprecht and Patashnick, Albany, New York, USA) operating from a

162 certified $PM_{2.5}$ inlet (also from Rupprecht and Patashnick). The total flow rate at the inlet was

163 16.7 L min^{-1} to ensure the correct functioning of the inlet, and the sampling flow rate driving

164 the aerosol-laden air to the microbalance was 3 L min^{-1}. The temperature of the sample stream

165 was kept constant at 50ºC.

166 Three-dimensional air mass back-trajectories are calculated using the NOAA HYbrid Single-

167 Particle Lagrangian Integrated Trajectory Model (HYSPLIT; Draxler and Rolph, 2015). The

168 model uses the 1°×1° latitude-longitude grid, reanalysis meteorological database. The 6-hourly

169 reanalysis archive data are generated by the NCEP's GDAS (NCEP: National Centers for

170 Environmental Prediction; GDAS: Global Data Assimilation System) wind field reanalysis.

171 Further information can be found at https://rda.ucar.edu/datasets/ds083.2/.

172 ERA-Interim reanalysis data (Dee, et al. 2011) from the European Center for Medium Range

173 Weather Forecast (ECMWF) are used in the analysis of synoptic scale circulation patterns

174 associated with the identified dominant air mass transport to Henties Bay. The 6 hourly (0, 6,

175 12, 18 UTC) analysis data (0.75 x 0.75 degrees) at mean sea level pressure (MSLP - variable

176 151.128) and the 500 hPa geopotential height (ZG500 -- variable 129.128) are used for this

177 study. Data sets were normalised (MSLP / 100 and ZG500 /100) using Climate Data Operators

178 (CDO) (Schulzweida et al., 2006) and plotted with 2 hPa and 10 hPa isobaric intervals for

179 MSLP and 500 hPa level, respectively.

180 Surface black carbon concentrations predicted by the Modern-Era Retrospective analysis for

181 Research and Applications, Version 2 (MERRA-2, Gelaro et al., 2017), sampled at HBAO and

182 at a number of other sites (Zuidema et al., 2016) are used for comparison.

183 The HTAP_V2 dataset is used for gridded emission of anthropogenic black carbon for the year

184 2010 (Janssens-Maenhout et al., 2015). It consists of 0.1° x 0.1° grid-maps. HTAP_V2 uses

185 nationally reported emissions combined with regional scientific inventories in the format of

186 sector-specific grid maps. The grid maps are complemented with EDGARv4.3 data for those

187 regions where data are absent. Anthropogenic activities producing black carbon aerosols

188 comprise aviation, transportation, energy production, industries, ship traffic, residential and

189 agricultural burning.

3. Results

3.1. Temporal variability of eBC concentrations

Figure 2 shows daily and monthly averages of the eBC concentrations measured at HBAO between July 2012 and December 2015. Daily averages excluded spikes and peak values occurring on short time scales, less than 1-2 hours, resulting from contamination of local activities (episodic traffic and occasional open fires for barbequing meat).

The daily mean average of 53 ($\pm$ 55) ng m^{-3} is in accordance with previous observations in remote locations of the world shown in Table 1 (Bodhaine, 1995; Andreae et al., 1995; Derwent et al., 2001; von Schneidemesser et al., 2009; Marinoni et al., 2010; Sheridan et al., 2016). Andreae et al. (1995) found eBC mass concentrations lower than 50 ng m^{-3} along a cruise transect at 19°S over the south east Atlantic between Brazil and Angola, except when approaching the African continent, when concentrations increased in the range 50-150 ng m^{-3}, indicating a strong continental influence in this otherwise pristine environment. Additional published research, also in Table 1, reports absorption coefficients that would lead to comparable eBC concentrations (Bodhaine, 1995; Clarke, 1989; Quinn et al., 1998). For contrast, eBC mass concentrations in lofted layers above the marine boundary layer in the range 0.1-6 µg m^{-3} were reported for aged biomass burning haze (Kirchstetter et al., 2003; Formenti et al., 2003; Eatough et al; 2003), and up to 5-40 µg m^{-3} for fresh biomass smoke plumes (Kirchstetter et al., 2003).

Figure 2 also shows an apparent seasonal variability in eBC, further highlighted by the monthly means and by the comparison with PM$_{2.5}$ mass concentration measurements performed at the site during 2013, which conversely, did not display any particular seasonal cycle (Figure S1), likely because dominated by sea salt. Concentrations increase in the austral winter from May to July, and decrease from August to April. The increase from May to July is well captured by the MERRA-2 reanalysis (also shown in Figure 2), according to which, however,

9

215 concentrations only start decreasing after September. The observed seasonality is somewhat

216 surprising in that it precedes the seasonal maximum of the biomass burning fire season in

217 southern Africa, peaking in the austral dry season from August to October (Swap et al., 2002).

218 As previously stated in this paragraph, data constituting the time series have been screened to

219 exclude short-term variability (less than one-two hour time intervals) to exclude isolated and

220 episodic sources. Peaks of eBC driving the seasonal increase in the May-to-August period are

221 long-lasting, extending between 6 and 11 hours, and occurring during both day- and night-time.

222 This suggests that transport is the cause of the seasonal peaks. The following section explores

223 this hypothesis and attempts the quantification of attribution of eBC peaks to specific transport

224 patterns.

225 **3.2. General atmospheric circulation driving air mass transport**

226 Transport to the west coast of Namibia is influenced by four general circulation patterns:

227 baroclinic westerly waves, barotropic easterly waves, the semi-permanent south Atlantic high

228 pressure and a continental high pressure circulation. The relative influence of each circulation

229 pattern is highly seasonal and driven by the meridional migration towards the north in austral

230 winter and to the south in summer. The origin of the air parcel over the southern ocean is linked

231 to the passage of a westerly wave and front that propagates towards the subcontinent form the

232 south west. These are Rossby waves that form as a result of the extratropical temperature

233 gradient with a maximum impact on the weather over southern Africa in winter. The easterly

234 waves are trade winds that are associated with the position of the Inter Tropical Convergence

235 Zone (ITCZ) that reaches a maximum over the subcontinent during summer (Tyson and

236 Preston-Whyte, 2014; Taljaard, 1994). The semi-permanent high pressure system (anticyclone)

237 results from the descending limb of the Hadley circulation that interacts with the

238 aforementioned waves. The south Atlantic high pressure system will ridges behind a passing

239 westerly wave in the direction of maximum cold air advection. Conversely, a strengthening

240   anticyclone will block propagations of these waves and induce a strong persistent continental

241   high pressure. Air masses reaching the sampling station have been found to originate from the

242   adjacent Atlantic Ocean and various locations over the continental subcontinent. Coastal lows

243   are induced along the west coast of Namibia and result in offshore flow ahead of westerly

244   waves. This low pressure system forms localised cyclonic circulation that includes onshore flow

245   in the north and offshore flow in the south of the low pressure cell (Tlhalerwa et al., 2005;

246   Tyson and Preston-Whyte, 2014).

247   **3.3. Identification of air mass transport pathways impacting HBAO**

248   Three-day back-trajectories calculated daily between July 2012 and December 2015 are

249   grouped according to the progression of the general synoptic circulation patterns and assigned

250   to 8 geographical sectors according to the position of their end point, shown in Figure 3. Four

251   sectors (G1 to G4) correspond to oceanic air masses and sectors (G5 to G7) to transport from

252   the continent. The last sector (G8) describes air masses recirculating around the sampling site

253   for most of the three day period. Figure 3 also shows the 2010 black carbon aerosol regional

254   emission HTAP_V2 inventory grid map from anthropogenic activities. Emissions are low in

255   Namibia and neighbouring countries as Botswana and the west-central South Africa. Areas of

256   higher emissions are Angola (with an hotspot in correspondence with the capital city Luanda),

257   costal South Africa, particularly to the east, but also to the south in the Cape Town greater area,

258   but mostly in the South African Highveld (27°S, 28°W) where the energy production is

259   concentrated. The open-ocean and coastal ship tracks are also evident.

260   The monthly distribution of fire counts from 2012 to 2015 provided by MODIS/Aqua is shown

261   in Figure 4. Although some interannual variability exists, the image record is consistent in

262   showing that the fire season in Southern African starts towards April and extends until October.

263   The major source areas are north of Namibia (Angola, Zambia), in South Africa (to the east and

264   along the south coast) and in Mozambique. In Namibia, fire counts are seen towards the north,

265   around the Etosha Pan desert.

266   The seasonal contribution of these air masses transport pathways is shown in Figure 5. Sectors

267   G1 to G4 represent the most common air flow pathway (73% out of 1279 calculated back-

268   trajectories). The Southern Atlantic Ocean transport (G1 and G2) is the dominant surface

269   circulation along the west coast, resulting from the northward moving limb of the surface south

270   Atlantic high pressure. Air masses originate over the southern Atlantic Ocean, as far south as

271   55°S (sector G2, representing approximately 66% of the air mass occurrences). During summer

272   this is predominantly a function of the most southerly location of the centre of the south Atlantic

273   high (Figure 6). In winter transport results from a complex interaction between the westerly

274   waves propagating from the south west over the subcontinent and the reestablishment of the

275   south Atlantic High in the westerly waves wake. Initially, air transport is towards the east and

276   is then directed northwards along the west coast to Namibia (Figure 7). The distance covered

277   by these air masses is several thousand kilometres due to the high wind speeds associated with

278   the initial transport in the cyclonic circulation.

279   Sectors G3 and G4 describe transport from the tropical regions of the Atlantic Ocean. The

280   onshore flow towards the sampling site forms as a westerly wave advances. A shallow, localised

281   cell of low pressure (cyclonic circulation) is induced along the west coast with a diameter of

282   approximately 200 km. Towards the north of the cell onshore flow occurs, while in the southern

283   portion of the cell the flow is offshore. This circulation has also been shown to induce the dust

284   plumes that blow off the Namibian coast over the Atlantic Ocean from ephemeral river beds

285   along the west coast of Namibia (Tlhalerwa et al., 2005). The low, referred to as a coastal low,

286   then propagates southwards behind the surface front. It is possible for air that is moved offshore

287   in the easterly wave over Angola to be caught up in this more near shore circulation.

288   Transport to HBAO from the continent (sectors G5-G7) occurred on 19% of the total days

289   (sectors G5, G6 and G7). These transport pathways are directly linked to the position of the

290   easterly wave over the subcontinent as well as the position of the trough line associated with

291   the wave. As pointed out earlier, the position of the easterly wave is highly seasonal. In general,

292   air is transported across the subcontinent and exits to the Atlantic Ocean in the westerly

293   transport. The low pressure trough moves across the subcontinent. The position of the trough

294   also determines the exact pathway of transport as well as the sector in which air masses

295   originate. If the trough is situated along the west coast it forms a west coast trough that

296   facilitates flow along and close to the west coast. During summer the easterly wave reaches to

297   the southern tip of southern Africa. This leads to transport of air from areas of South Africa,

298   including the highly industrialised Highveld region (Figure 8a). In winter the easterly wave

299   seldom reaches south of 25°S. Air masses during this season are more likely to originate over

300   the central portion of southern Africa (Figure 8b).

301   Finally, sector G8 is associated with air masses originating within 100 km of HBAO (Figure

302   9), either from land or from the ocean, and representing about 8% of the air mass occurrences

303   (Figure 5). This circulation, only occurring in the second half of each year (Figure 5), is linked

304   to the formation of a low pressure heat cell close to the west coast of Namibia centred at about

305   the latitude of Henties Bay. Despite this being cyclonic flow the circulation is closed (Figure 9)

306   and therefore represents transport from close to the sampling site. The heat low is always

307   embedded in an easterly wave or west coast trough. Centres of low pressure form along the

308   west coast producing local and mesoscale circulation from the interior of Namibia to the coast.

309   This flow pattern is distinguishable from a coastal low as it is centred on the subcontinent

310   whereas the coastal low is always centred on the coast just offshore.

3.4. Contribution of air transport patterns to the measured eBC

Figure 10 illustrates the contribution of the air mass sectors G1-G8 to the eBC mass concentrations measured at HBAO and those estimated by the MERRA-2 reanalysis. This has been done by calculating the distribution of eBC values per group.

Although the absolute values differ by a factor of 2-3, measurements and reanalysis show some consistent temporal features. Episodic high values of eBC concentrations occur independently on the origin of the air mass. The southern Atlantic oceanic air masses (sectors G1, G2 and G3) and the continental G7 sector, corresponding to the low population density semi-arid region of the Karoo, in South Africa, display the lowest concentrations. In particular, the oceanic sectors are characterised by a south-to-north gradient, the highest mean concentrations being from sectors G4, offshore northern Namibia and Angola, comparable to those from the continental sectors G5 and G6, and G8, representing recirculating air masses. Measurements at HBAO indicate that the contributions of sectors G5 and G6 are equivalent, while sector G5 is the largest contributor according to the MERRA-2 reanalysis.

4. Discussion and conclusions

This papers present the first long-term time series of equivalent black carbon concentrations in the marine boundary layer on the south-east Atlantic coast offshore southern Africa. Observations were conducted at the Henties Bay Aerosol Observatory, in Namibia, between July 2012 and December 2015.

Higher concentrations of eBC on the western coast of southern Africa are observed from April to July within continental and marine air masses north of 30°S (sectors G4, G5 and G6). Daily eBC peak concentrations at HBAO do not exceed 800 ng m^{-3}, and are seldom larger than 200 ng m^{-3}, lower than measured at Ascension Island, approximately 1500 kilometres downwind of coastal Namibia and located along the main outflow pathway from southern Africa to the

335   Atlantic Ocean (Swap et al., 1996; 2002; Adebiyi and Zuidema, 2016; Zuidema et al., 2018).

336   The seasonality of the eBC concentrations observed at HBAO corresponds to the seasonal shift

337   from southern to northern circulation at the surface, and is in phase with the April onset of the

338   fire season in southern Africa (Figure 5). The seasonal increase at HBAO is also well captured

339   by the MERRA-2 reanalysis model, but it occurs earlier than reported by Zuidema et al. (2018)

340   at Ascension Island (June to August). This seems to indicate that HBAO is on a minor branch

341   of the transport pathway of the continental biomass burning smoke plume from continental

342   southern Africa compared with the biomass burning plumes that reach Ascension Island. The

343   MERRA-2 reanalysis shows higher concentrations than measured at HBAO and suggests that

344   the period of high concentrations should persist until September rather than August as in the

345   HBAO measurements. This points out to the inherent degree of uncertainty in our estimates.

346   The correction factors (filter loading and multiple scattering corrections) needed to convert the

347   measured attenuation into a value eBC concentration are assumed and not evaluated from

348   concurrent measurements, and set to fixed values as the aerosol at HBAO would derive from a

349   single source type. We do not deal either with potential changes of the aerosol properties due

350   to ageing. Differences could also be due to the representation of the timing and extent of a

351   southward shift of the easterly during summer. Although these issues cannot be resolved with

352   the present dataset, they question the representation of the transport of smoke plumes at the

353   subcontinental scale of southern Africa.

354   There is no doubt that the transport of wildfire smoke is the major regional source of the eBC

355   aerosols for the western coast of Namibia. However, the presence of episodic outliers and the

356   relatively elevated concentrations observed for oceanic air masses originating south of HBAO

357   (sectors G1 to G3 in Figure 7) suggests that additional sources could contribute to the load of

358   light-absorbing aerosols in the marine boundary layer. In particular, the contribution of the

359   coastal and open ocean maritime shipping routes in the south Atlantic ocean (Tournadre, 2014;

360   Fraser et al., 2016; Johannson et al., 2017), and that of long-range continental anti-cyclonic

361   transport from the industrial areas of the South African Highveld, showing up in Figure 3

362   (Piketh et al., 2002), should be further explored.

363   By the very rough assumption of the mass fraction of black carbon to the total fine aerosol

364   (10%, Bond et al., 2013), we estimate that the mean fine mass of aerosols containing eBC would

365   be 0.5 ($\pm$ 0.5) μg m^{-3}. For comparison, the mean PM$_{2.5}$ mass concentration at HBAO was 14 ($\pm$

366   11) μg m^{-3} in 2013 (Figure S1).

367   These aerosols below clouds would have a negligible direct radiative effect. There are almost

368   no AERONET measurements of the aerosol optical depth (AOD) at HBAO concurrent to the

369   eBC data series. However, Figure S2 shows the time series of the AERONET level 2.0 AOD

370   of the fine and coarse mode aerosols (AOD$_F$ and AOD$_C$) evaluated by the O'Neill et al. (2003)

371   algorithm between December 2011 and May 2012, and then from May to December 2015.

372   Figure S2 shows that the AOD$_F$ varies significantly from background values in the December

373   2011-May 2012 period (average 0.05 $\pm$ 0.03) to peak values of 0.4 and higher during August,

374   September and October 2015, when the transport of biomass burning occurs in the free

375   troposphere (Swap et al., 2003). The AOD$_C$, contributed essentially by sea salt, is relatively

376   invariant with time. There is no process other than biomass burning that would inject aerosols

377   above the marine boundary layer, henceforth we can consider the mean value for December

378   2011-May 2012 as a reasonable evaluation of the optical depth of the fine mode of aerosols

379   below clouds, including eBC.

380   The eBC aerosols might act on the microphysical properties of the local stratocumulus clouds.

381   At Ascension Island, Zuidema et al. (2018) demonstrated the good correlation between the

382   concentrations of refractory black carbon and cloud condensation nuclei (CCN) at

383   supersaturations exceeding 0.2%. A similar effect should be expected at HBAO and could be

384   important, outside but also during the biomass burning season as the entrainment of biomass

burning aerosols from the free troposphere maybe be inhibited by the thermal inversions clear air slots separating the elevated plumes and the marine boundary layer (Keil and Haywood, 2003; Haywood et al., 2003; Hobbs et al., 2003). Finally, by deposition, these low-level aerosols could act on the biological activity for the oligotrophic south Atlantic gyre in summer, providing with soluble nutrient species, such as dissolved nitrogen, phosphorous, and iron (Guieu et al., 2005; Luo et al., 2008; Paris et al., 2010).

In conclusion, the chemical apportionment of the AOD_F below cloud and the hygroscopic properties of the eBC aerosols at HBAO deserves exploration by future refined experiments.

Data availability

Original data for measured light-attenuation at HBAO are distributed by the French national AERIS data center (https://www.aeris-data.fr/direct-access-icare-2/). Treated data can be obtained by email request to the first author of this paper.

Author contributions

Paola Formenti, Stuart John Piketh, Andreas Namwoonde, Samuel Mafwila, Edosa Omoregie, Wolfgang Yunkermann and Willy Maenhaut designed the experiments and the sampling site.

Paola Formenti, Stuart John Piketh, Andreas Namwoonde, Mathieu Cazaunau, Anaïs Feron, Cécile Gaimoz, Stephen Broccardo, Nicola Walton, Karine Desboeufs, and Mattheus Hanghome performed the experiments.

Paola Formenti and Stuart John Piketh performed the full data analysis with contributions by Danitza Klopper, Guillaume Siour, and Roelof Burger.

Paola Formenti, Stuart Piketh, Danitza Klopper and Roelof Burger wrote the paper with comments from all co-authors.

Competing interests

The authors declare that they have no conflict of interest.

432   **References**

433   Adebiyi, A., and P. Zuidema, The role of the southern African easterly jet in modifying the
434   southeast Atlantic aerosol and cloud environments. Q. J. Roy. Meteor. Soc., 142, 1574–
435   1589, doi: 10.1002/qj.2765, 2016.

436   Andreae, M. O., W. Elbert, and S. J. de Mora, Biogenic sulfur emissions and aerosols over the
437   tropical South Atlantic: 3. Atmospheric dimethylsulfide, aerosols and cloud
438   condensation nuclei, J. Geophys. Res. Atmos., 100(D6), 11335-11356, 1995.

439   Andreae, M. O., J. Fishman, and J. Lindesay, The Southern Tropical Atlantic Region
440   Experiment (STARE): Transport and Atmospheric Chemistry near the Equator-Atlantic
441   (TRACE A) and Southern African Fire-Atmosphere Research Initiative (SAFARI): An
442   introduction, J. Geophys. Res., 101(D19), 23519–23520, doi: 10.1029/96JD01786,
443   1996.

444   Arnott, W., Hamasha, K., Moosm¨uller, H., Sheridan, P. J. , and Ogren, J. A.: Towards aerosol
445   light-absorption measurements with a 7-wavelength aethalometer: Evaluation with a
446   photoacoustic instrument and 3-wavelength nephelometer, Aerosol Sci Tech., 39(1),
447   17–29, 2005.

448   Bodhaine, B. A., Aerosol absorption measurements at Barrow, Mauna Loa, and South Pole, J.
449   Geophys. Res., 100, 8967–8975, 1995.

450   Bond, T. and R. W. Bergstrom, Light Absorption by Carbonaceous Particles: An Investigative
451   Review, Aerosol Sci. Technol., 39:1–41, doi: 10.1080/02786820500421521, 2006.

452   Bond, T. C., S. J. Doherty, D. W. Fahey, P.M. Forster, T. Berntsen, B. J. DeAngelo, M. G.
453   Flanner, S. Ghan, B. Kärcher, D. Koch, S. Kinne, Y. Kondo, P. K. Quinn, M. C. Sarofim,
454   M. G. Schultz,   M. Schulz, C. Venkataraman, H. Zhang, S. Zhang, N. Bellouin,
455   S. K. Guttikunda, P. K. Hopke, M. Z. Jacobson, J.W. Kaiser, Z. Klimont, U. Lohmann,
456   J. P. Schwarz, D. Shindell, T. Storelvmo, S. G. Warren and C. S. Zender, Bounding the
457   role of black carbon in the climate system: A scientific assessment, J. Geophys. Res.
458   Atmos., 118, 5380–5552, doi:10.1002/jgrd.50171, 2013.

459   Boucher, O., D. Randall, P. Artaxo, C. Bretherton, G. Feingold, P. Forster, V.-M. Kerminen,
460   Y. Kondo, H. Liao, U. Lohmann, P. Rasch, S.K. Satheesh, S. Sherwood, B. Stevens and
461   X.Y. Zhang, 2013: Clouds and Aerosols. In: Climate Change, The Physical Science
462   Basis. Contribution of Working Group I to the Fifth Assessment Report of the
463   Intergovernmental Panel on Climate Change [Stocker, T.F., D. Qin, G.-K. Plattner, M.
464   Tignor, S.K. Allen, J. Boschung, A. Nauels, Y. Xia, V. Bex and P.M. Midgley (eds.)].
465   Cambridge University Press, Cambridge, United Kingdom and New York, NY, USA,
466   pp. 571–658, doi:10.1017/CBO9781107415324.016, 2013.

467   Caponi, L., P. Formenti, D. Massabó, C. Di Biagio, M. Cazaunau, E. Pangui, S. Chevaillier, G.
468   Landrot, M. O. Andreae, K. Kandler, S. J. Piketh, T. Saeed, D. Seibert, E. Williams, Y.
469   Balkanski, P. Prati, and J. Doussin, Spectral- and size-resolved mass absorption
470   efficiency of mineral dust aerosols in the shortwave spectrum: a simulation chamber
471   study, Atmos. Chem. Phys. Discuss., 17, pp. 7175–7191, doi: doi.org/10.5194/acp-17-
472   7175-2017, 2017.

473   Chung, S. H. and J. H. Seinfeld, Global distribution and climate forcing of carbonaceous
474   aerosols, J. Geophys. Res. Atmos., 107(D19), AAC 14-11-AAC 14-33, 2002.

Clarke, A. D.: Aerosol Light Absorption by Soot in Remote Environments, Aerosol Sci. Technol., 10, 161-171, 10.1080/02786828908959231, 1989.

Collaud Coen, M., Weingartner, E., Apituley, A., Ceburnis, D., Fierz-Schmidhauser, R., Flentje, H., Henzing, J. S., Jennings, S. G., Moerman, M., Petzold, A., Schmid, O., and Baltensperger, U.: Minimizing light absorption measurement artifacts of the Aethalometer: evaluation of five correction algorithms, Atmos. Meas. Tech., 3, 457-474, 10.5194/amt-3-457-2010, 2010.

Cook, C., Reason, C.J.C. and B.C. Hewitson, Wet and dry spells within particularly wet and dry summers in the South African summer rainfall region. Climate Res., 26(1), 17–31, 2004.

Dee, D.P., Uppala, S.M., Simmons, A.J., Berrisford, P., Poli, P., Kobayashi, S., Andrae, U., Balmaseda, M.A., Balsamo, G., Bauer, D.P. and Bechtold, P., The ERA Interim reanalysis: Configuration and performance of the data assimilation system. Q. J. Royal Met. Soc., 137(656),.553-597, 2011.

Derwent, R. G., D. B. Ryall, S. G. Jennings, T. G. Spain, and P. G. Simmonds, Black carbon aerosol and carbon monoxide in European regionally polluted air masses at Mace Head, Ireland during 1995-1998, Atmos. Environ., 35, 6371-6378, 2001.

Draxler, R. R. and G. D. Rolph, HYSPLIT (HYbrid Single-Particle Lagrangian Integrated Trajectory) Model access via NOAA ARL READY Website (http://ready.arl.noaa.gov/HYSPLIT.php). NOAA Air Resources Laboratory, Silver Spring, MD, 2015.

Eatough, D. J., N. L. Eatough, Y. Pang, S. Sizemore, T. W. Kirchstetter, T. Novakov, and P. V. Hobbs, Semivolatile particulate organic material in southern Africa during SAFARI 2000, J. Geophys. Res., 108, 8479, doi:10.1029/2002JD002296, D13, 2003.

Flato, G., et al. (2013), Evaluation of climate models, in Climate Change: The Physical Science Basis. Contribution of Working Group I to the Fifth Assessment Report of the Intergovernmental Panel on Climate Change, edited by T. F. Stocker et al., pp. 741–866, Cambridge Univ. Press, Cambridge, U. K., and New York, doi:10.1017/CBO9781107415324.020, 2013.

Formenti, P., S. J. Piketh and H. J. Annegarn, Detection of non-sea salt sulphate aerosol at a remote coastal site in South Africa: A PIXE study, Nuclear Instruments and Methods in Physics Research B, 150, 332–338, doi: 10.1016/S0168-583X(98)01041-6, 1999.

Formenti, P., W. Elbert, W. Maenhaut, J. Haywood, S. Osborne, and M. O. Andreae, Inorganic and carbonaceous aerosols during the Southern African Regional Science Initiative (SAFARI 2000) experiment: Chemical characteristics, physical properties, and emission data for smoke from African biomass burning, J. Geophys. Res., 108, 8488, doi:10.1029/2002JD002408, 2003.

Fraser, D. R., T. Notteboom, and C. Ducruet, Peripherality in the global container shipping network: the case of the Southern African container port system, GeoJournal, 81, 139. doi:10.1007/s10708-014-9610-6, 2016.

Gelaro, R., W. McCarty, M.J. Suárez, R. Todling, A. Molod, L. Takacs, C.A. Randles, A. Darmenov, M.G. Bosilovich, R. Reichle, K. Wargan, L. Coy, R. Cullather, C. Draper, S. Akella, V. Buchard, A. Conaty, A.M. da Silva, W. Gu, G. Kim, R. Koster, R. Lucchesi, D. Merkova, J.E. Nielsen, G. Partyka, S. Pawson, W. Putman, M. Rienecker, S.D. Schubert, M. Sienkiewicz, and B. Zhao, The Modern-Era Retrospective Analysis

for Research and Applications, Version 2 (MERRA-2). J. Climate, 30, 5419–5454, https://doi.org/10.1175/JCLI-D-16-0758.1, 2017.

Guieu, C., S. Bonnet, T. Wagener and M. D. Loye-Pilot 2005), Biomass burning as a source of dissolved iron to the open ocean?, Geophys. Res. Lett., 32, L19608, doi:10.1029/2005GL022962.

Hansen, A. D. A., The aethalometer, technical guide, 2005; available online at http://www.mageesci.com/images/stories/docs/Aethalometer_book_2005.07.03.pdf.

Hansen, A. D. A., H. Rosen and T. Novakov, The aethalometer - an instrument for the real-time measurement of optical absorption by aerosol particles, Sci. Total Environ., 36, 191, 1984.

Hansen, J. E., Sato, M. and Ruedy, R., Radiative forcing and climate response, J. Geophys. Res., 102, 6831–6864, 1997.

Haywood, J., and K. Shine, The effect of anthropogenic sulfate and soot aerosol on the clear sky planetary radiation budget, Geophys. Res. Lett., 22(5), 603-606, 1995.

Haywood, J. M., S. R. Osborne, P. N. Francis, A. Keil, P. Formenti, M. O. Andreae, and P. H. Kaye, The mean physical and optical properties of regional haze dominated by biomass burning aerosol measured from the C-130 aircraft during SAFARI 2000, J. Geophys. Res., 108 (D13), 8473, doi:10.1029/2002JD002226, 2003.

Hobbs, P. V. (2003), Clean air slots and dense atmospheric pollution in southern Africa, J. Geophys. Res., 108, 8490, doi:10.1029/2002JD002156, D13.

Jacobson, M., Strong radiative heating due to the mixing state of black carbon in atmospheric aerosols, Nature, 409(6821), 695-697, 2001.

Janssens-Maenhout, G., Crippa, M., Guizzardi, D., Dentener, F., Muntean, M., Pouliot, G., Keating, T., Zhang, Q., Kurokawa, J., Wankmüller, R., Denier van der Gon, H., Kuenen, J. J. P., Klimont, Z., Frost, G., Darras, S., Koffi, B., and Li, M.: HTAP_v2.2: a mosaic of regional and global emission grid maps for 2008 and 2010 to study hemispheric transport of air pollution, Atmos. Chem. Phys., 15, 11411-11432, 2015.

Johansson, L., Jalkanen, J.-P., and Kukkonen, J.: Global assessment of shipping emissions in 2015 on a high spatial and temporal resolution, Atmos. Environ., 167, 403-415, https://doi.org/10.1016/j.atmosenv.2017.08.042, 2017.

Keil, A., and J. M. Haywood, Solar radiative forcing by biomass burning aerosol particles during SAFARI 2000: A case study based on measured aerosol and cloud properties, J. Geophys. Res., 108, 8467, doi:10.1029/2002JD002315, D13, 2003.

Kirchstetter, T. W., T. Novakov, P. V. Hobbs, and B. Magi, Airborne measurements of carbonaceous aerosols in southern Africa during the dry biomass burning season, J. Geophys. Res., 108, 8476, doi:10.1029/2002JD002171, D13, 2003.

Kirchstetter, T. W., T. Novakov, and P. V. Hobbs, Evidence that the spectral dependence of light absorption by aerosols is affected by organic carbon, J. Geophys. Res., 109, D21208, doi:10.1029/2004JD004999, 2004.

Knox, A., G. J. Evans, J. R. Brook, X. Yao, C. H. Jeong, K. J. Godri, K. Sabaliauskas, and J. G. Slowik, Mass Absorption Cross-Section of Ambient Black Carbon Aerosol in Relation to Chemical Age, Aerosol Sci. Technol., 43(6), 522-532, 2009.

Koch, D. and A. D. Del Genio, Black carbon semi-direct effects on cloud cover: review and synthesis, Atmos. Chem. Phys., 10, 7685-7696, doi:10.5194/acp-10-7685-2010, 2010.

564 Liousse, C., H. Cachier and S. G. Jennings, Optical and thermal measurements of black carbon
565   aerosol content in different environments: Variations of the specific attenuation cross-
566   section, sigma (σ). Atmos. Environ., 27A(8), 1203-1211, doi: 10.1016/0960-
567   1686(93)90246-U, 1993.

568 Marinoni, A., P. Cristofanelli, P. Laj, R. Duchi, F. Calzolari, S. Decesari, K. Sellegri, E.
569   Vuillermoz, G. P. Verza, P. Villani, and P. Bonasoni, Aerosol mass and black carbon
570   concentrations, a two year record at NCO-P (5079 m, Southern Himalayas), Atmos.
571   Chem. Phys., 10, 8551-8562, doi:10.5194/acp-10-8551-2010, 2010.

572 Martins, J. V., P. Artaxo, C. Liousse, J. S. Reid, P. V. Hobbs, Y. J. Kaufman, Effects of black
573   carbon content, particle size and mixing on light absorption by aerosol particles from
574   biomass burning in Brazil, J. Geophys. Res., 103, D24, 32041-32050, 1998.

575 Maúre, G., Pinto, I., Ndebele-Murisa, M., Muthige, M., Lennard, C., Nikulin, G., Dosio, A.,
576   and Meque, A., The southern African climate under 1.5 °C and 2 °C of global warming
577   as simulated by CORDEX regional climate models, Environ. Res. Lett., 13, 065002,
578   2018.

579 Myhre, G., Samset, B. H., Schulz, M., Balkanski, Y., Bauer, S., Berntsen, T. K., Bian, H.,
580   Bellouin, N., Chin, M., Diehl, T., Easter, R. C., Feichter, J., Ghan, S. J., Hauglustaine,
581   D., Iversen, T., Kinne, S., Kirkevåg, A., Lamarque, J. F., Lin, G., Liu, X., Lund, M. T.,
582   Luo, G., Ma, X., van Noije, T., Penner, J. E., Rasch, P. J., Ruiz, A., Seland, Ø., Skeie,
583   R. B., Stier, P., Takemura, T., Tsigaridis, K., Wang, P., Wang, Z., Xu, L., Yu, H., Yu,
584   F., Yoon, J. H., Zhang, K., Zhang, H., and Zhou, C.: Radiative forcing of the direct
585   aerosol effect from AeroCom Phase II simulations, Atmos. Chem. Phys., 13, 1853-1877,
586   10.5194/acp-13-1853-2013, 2013.

587 O'Neill, N. T.,T. F., Eck, , A. Smirnov, B. N.Holben, S. Thulasiraman, Spectral discrimination
588   of coarse and fine mode optical depth, 108, J. Geophys. Res., No. D17, 4559-4573,
589   10.1029/2002JD002975, 2003.

590 Paris, P., K. V. Desboeufs, P. Formenti, S. Nava, and C. Chou (2010), Chemical
591   characterisation of iron in Dust and Biomass burning aerosols during AMMA-
592   SOP0/DABEX: implication on iron solubility, Atmos. Chem. Phys., 10, 4273–4282.

593 Petzold, A., C. Kopp, and R. Niessner, The dependence of the specific attenuation cross-section
594   on black carbon mass fraction and particle size, Atmos. Environ., 31(5), 661-672, 1997.

595 Piketh, S. J., H. J. Annegarn and P. D. Tyson, Lower tropospheric aerosol loadings over South
596   Africa: The relative contribution of aeolian dust, industrial emissions, and biomass
597   burning, J. Geophys. Res., 104, 1597. doi: 10.1029/1998JD100014, 1999.

598 Piketh, S. J., R. J. Swap, W. Maenhaut, H. J. Annegarn, and P. Formenti, Chemical evidence of
599   long-range atmospheric transport over southern Africa, J. Geophys. Res., 107(D24),
600   4817, doi:10.1029/2002JD002056, 2002.

601 Quinn, P. K., Coffman, D. J., Kapustin, V. N., Bates, T. S., and Covert, D. S.: Aerosol optical
602   properties in the marine boundary layer during the First Aerosol Characterization
603   Experiment (ACE 1) and the underlying chemical and physical aerosol properties, J.
604   Geophys. Res. Atmos., 103, 16547-16563, doi:10.1029/97JD02345, 1998.

605 Saturno, J., Pöhlker, C., Massabò, D., Brito, J., Carbone, S., Cheng, Y., Chi, X., Ditas, F., Hrabě
606   de Angelis, I., Morán-Zuloaga, D., Pöhlker, M. L., Rizzo, L. V., Walter, D., Wang, Q.,
607   Artaxo, P., Prati, P., and Andreae, M. O.: Comparison of different Aethalometer
608   correction schemes and a reference multi-wavelength absorption technique for ambient

609 aerosol data, Atmos. Meas. Tech., 10, 2837-2850, https://doi.org/10.5194/amt-10-2837-
610   2017, 2017.

611 Schmid, O., Artaxo, P., Arnott,W. P., Chand, D., Gatti, L. V., Frank, G. P., Hoffer, A.,
612   Schnaiter, M., and Andreae, M. O.: Spectral light absorption by ambient aerosols
613   influenced by biomass burning in the Amazon Basin. I: Comparison and field calibration
614   of absorption measurement techniques, Atmos. Chem. Phys., 6, 3443–3462, 2006,

615 Schulzweida, U., L. Kornblueh, and R. Quast, CDO user's guide, Climate Data Operators,
616   Version, 1(6), 2006.

617 Segura, S., Estellés, V., Titos, G., Lyamani, H., Utrillas, M. P., Zotter, P., Prévôt, A. S. H.,
618   Mocnik, G., Alados-Arboledas, L., and Martínez-Lozano, J. A.: Determination and
619   analysis of in situ spectral aerosol optical properties by a multi-instrumental approach,
620   Atmos. Meas. Tech., 7, 2373–2387, https://doi.org/10.5194/amt-7-2373-2014, 2014.

621 Seinfeld, J. H. and S. N. Pandis, Eds., Atmospheric chemistry and physics: From air pollution
622   to climate change. New York, John Wiley and Sons, Inc., 1997.

623 Sheridan, P., E. Andrews, L. Schmeisser, B. Vasel, J. Ogren, Aerosol Measurements at South
624   Pole: Climatology and Impact of Local Contamination, Aerosol and Air Quality
625   Research, 16: 855–872, doi: 10.4209/aaqr.2015.05.0358, 2016.

626 Subramanian, R., G. L. Kok, D. Baumgardner, A. Clarke, Y. Shinozuka, T. L. Campos, C. G.
627   Heizer, B. B. Stephens, B. de Foy, P. B. Voss, and R. A. Zaveri, Black carbon over
628   Mexico: the effect of atmospheric transport on mixing state, mass absorption cross-
629   section, and BC/CO ratios, Atmos. Chem. Phys., 10, 219-237, doi:10.5194/acp-10-219-
630   2010, 2010.

631 Swap, R., M. Garstang, S. A. Macko, P. D. Tyson, W. Maenhaut, P. Artaxo, P. Kållberg and R.
632   Talbot, The long-range transport of southern African aerosols to the tropical South
633   Atlantic, J. Geophys. Res., 101, 23777–23791, doi: 10.1029/95JD01049, 1996.

634 Swap, R. J., H. J. Annegarn, J. T. Suttles, J. Haywood, M. C. Helmlinger, C. Hely, P. V. Hobbs,
635   B. N. Holben, J. Ji, M. D. King, T. Landmann, W. Maenhaut, L. Otter, B. Pak, S. J.
636   Piketh, S. Platnick, J. Privette, D. Roy, A. M. Thompson, D. Ward, D. and R. Yokelson,
637   The Southern African Regional Science Initiative (SAFARI 2000) : overview of the dry
638   season field campaign, S. African J. Sci., 98, 125-130, 2002.

639 Taljaard, J. J., Atmospheric circulation systems, synoptic climatology and weather phenomena
640   of South Africa. Part 1: controls of the weather and climate of South Africa, Technical
641   Paper No. 27, Weather Bureau, Pretoria, 1994 (available from South African Weather
642   Bureau, Private Bag X097, Pretoria 0001).

643 Tlhalerwa, K., Freiman, M.T. and Piketh, S.J., Aerosol Deposition off the Southern African
644   West Coats by Berg Winds, S. African J. Sci., 87, 152-161, 2005.

645 Tournadre, J., Anthropogenic pressure on the open ocean: The growth of ship traffic revealed
646   by altimeter data analysis, Geophys. Res. Lett., 41, 7924-7932, 2014.

647 Tyson, P. D. and R. A. Preston-Whyte, The Weather and Climate of Southern Africa, 2nd ed.
648   Oxford University Press Southern Africa, Cape Town, 2014.

649 von Schneidemesser, E., J. J. Schauer, G. W. Hagler, and M. H. Bergin, Concentrations and
650   Sources of Carbonaceous Aerosol in the Atmosphere of Summit, Greenland, Atmos.
651   Environ., 43, 4155-4162, 2009.

652 Weingartner, E., H. Saathoff, M. Schnaiter, N. Streit, B. Bitnar, and U. Baltensperger,
653   Absorption of light by soot particles: determination of the absorption coefficient by
654   means of aethalometers, J. Aerosol Sci., 34, 1445-1463, 2003.

655 Zanatta, M., Gysel, M., Bukowiecki, N., Müller, T., Weingartner, E., Areskoug, H., Fiebig, M.,
656   Yttri, K. E., Mihalopoulos, N., Kouvarakis, G., Beddows, D., Harrison, R. M., Cavalli,
657   F., Putaud, J. P., Spindler, G., Wiedensohler, A., Alastuey, A., Pandolfi, M., Sellegri,
658   K., Swietlicki, E., Jaffrezo, J. L., Baltensperger, U., and Laj, P.: A European aerosol
659   phenomenology-5: Climatology of black carbon optical properties at 9 regional
660   background sites across Europe, Atmos. Environ, 145, 346-364,
661   https://doi.org/10.1016/j.atmosenv.2016.09.035, 2016.

662 Zuidema, P., Redemann, J., Haywood, J., Wood, R., Piketh, S., Hipondoka, M., and Formenti,
663   P.: Smoke and Clouds above the Southeast Atlantic: Upcoming Field Campaigns Probe
664   Absorbing Aerosol's Impact on Climate, Bull. American Met. Soc., 97, 1131-1135,
665   doi:10.1175/BAMS-D-15-00082.1, 2016.

666 Zuidema, P., Sedlacek, A. J., Flynn, C., Springston, S., Delgadillo, R., Zhang, J., Aiken, A. C.,
667   Koontz, A., and Muradyan, P.: The Ascension Island boundary layer in the remote
668   Southeast Atlantic is often smoky, Geophys. Res. Lett., 45, 4456-4465,
669   doi:10.1002/2017GL076926, 2018.

670 **Table captions**

671 **Table 1.** Values of mass concentrations of equivalent black carbon (eBC) from measurements

672 published in the literature for remote regions worldwide. When available, the specific

673 attenuation used to convert the measured attenuation to eBC is also reported.

674 **Figure captions**

675 **Figure 1:** Geographical location of the Henties Bay Aerosol Observatory (HBAO).

676 **Figure 2.** Comparisons of the time series of daily eBC mass concentrations (ng m-3) measured

677 at HBAO and predicted by the MERRA-2 reanalysis. The insert shows the respective monthly

678 variability by the box and whisker plot representation.

679 **Figure 3.** Geographical boundaries of the sectors used to classify the air mass back trajectories

680 superimposed to the emission grid-maps at 0.1° x 0.1° degrees of black carbon aerosols from

681 anthropogenic activities for the year 2010 provided by the HTAP_V2 inventory. Emissions are

682 expressed in Tons.

683 **Figure 4**. Fire counts per pixels from MODIS/Aqua provided by the NASA Fire Information

684 for Resources Management System (FIRMS). Colours range from yellow (1 fire count per

685 pixel) to red (+100 fire count per pixel). The underlying image is the corrected reflectance (true

686 colour) measured by MODIS/Aqua on the first day of each months.

687 **Figure 5**. Seasonal variation in the transport pathways of air masses reaching HBAO between

688 2012 and 2015.

689 **Figure 6**. Case study of mean sea level pressure over the sub-continent and adjacent South

690 Atlantic Ocean for 16-19 November 2014 illustrating the synoptic circulation that results in the

691 transport of air masses from sector G1.

692 **Figure 7**. Case study of mean sea level pressure over the sub-continent and adjacent South

693 Atlantic Ocean for 1-4 June 3013 illustrating the synoptic circulation that results in the

694 transport of air masses from sector G2.

695 **Figure 8**. Case study of mean sea level pressure over the sub-continent and adjacent south

696 Atlantic ocean for A) summer (10-13 December 2013) and B) winter (6-10 July 2013)

697 illustrating the synoptic circulation that results in the transport of air masses from sector G5-

698 G7.

699 **Figure 9**. Case study of mean sea level pressure over the sub-continent and adjacent South

700 Atlantic Ocean for 13-16 December 2012 illustrating the synoptic circulation that results in the

701 transport of air masses from sector G8.

702 **Figure 10**. Contribution of air mass sectors to the eBC concentrations at HBAO from (a) our

703 measurements and (b) MERRA-2 reanalysis.

704

705   **Table 1.** Values of mass concentrations of equivalent black carbon (eBC) from measurements

706   published in the literature for remote regions worldwide. When available, the specific

707   attenuation σ_{BC} used to convert the measured attenuation to eBC is also reported.

708

Location	eBC (ng m^{-3})	σ_{BC}, 880 nm (m^2 g^{-1})	Reference
Tropical South Atlantic off southern Africa, 19°S	50-150	10	Andreae et al. (1995)
Nepal Climate Observatory Pyramid, Himalaya	160 ± 296	6.5[$]	Marinoni et al. (2010)
Summit, Greenland	<340	-----	von Schneidemesser et al. (2009)
Mace-Head, Ireland	47-74	11 ± 3	Derwent et al. (2001)
South Pole, Antarctica	0.01-50	19	Bodhaine (1995)

709   [$] At 635 nm – measurements were conducted with a Multi-Angle absorption Photometer
710   (MAAP 5012, Thermo Electron Corporation).
711

712 **Figure 1:** Geographical location of the Henties Bay Aerosol Observatory (HBAO).

713

714

715   **Figure 2.** Comparisons of the time series of daily eBC mass concentrations (ng m-3) measured

716   at HBAO and predicted by the MERRA-2 reanalysis. The insert shows the respective monthly

717   variability by the box and whisker plot representation.
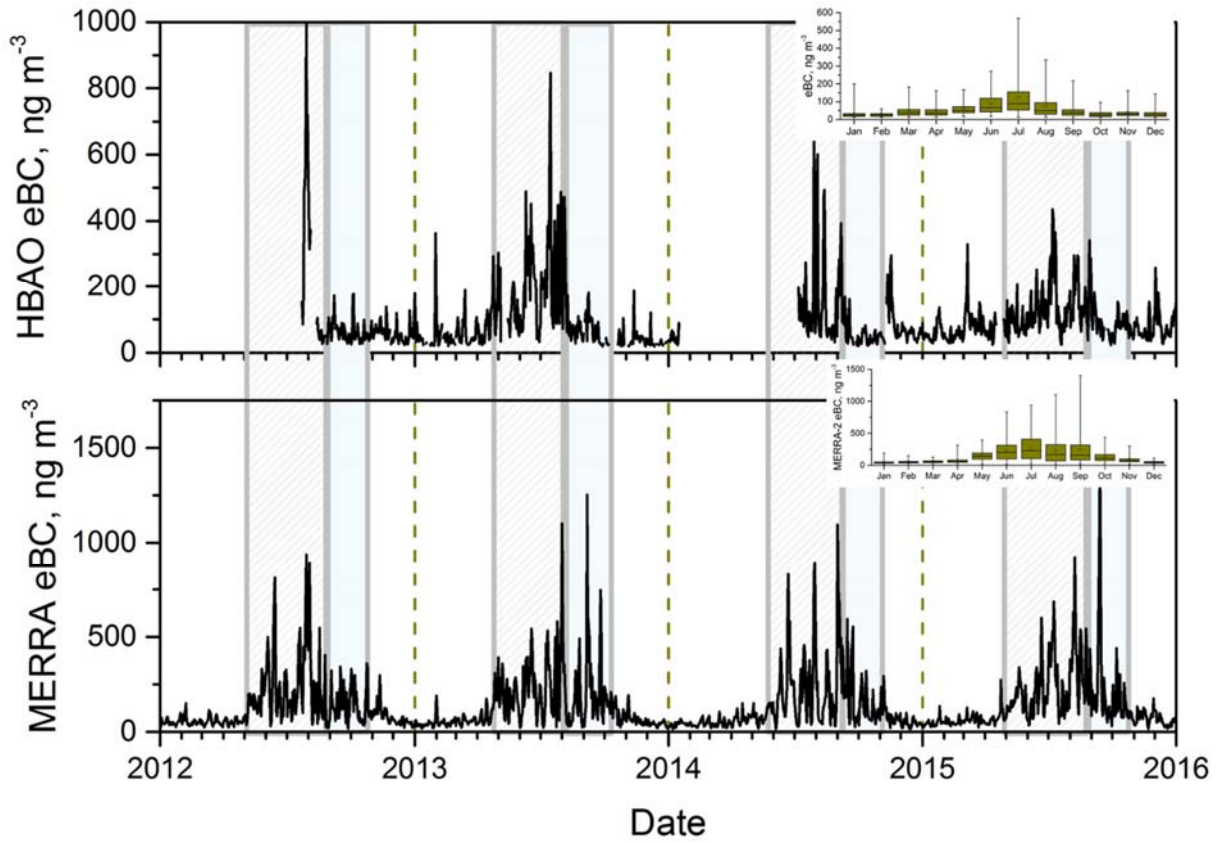
718

719

720 **Figure 3.** Geographical boundaries of the sectors used to classify the air mass back trajectories

721 superimposed to the emission grid-maps at 0.1° x 0.1° degrees of black carbon aerosols from

722 anthropogenic activities for the year 2010 provided by the HTAP_V2 inventory. Emissions are

723 expressed in Tons.
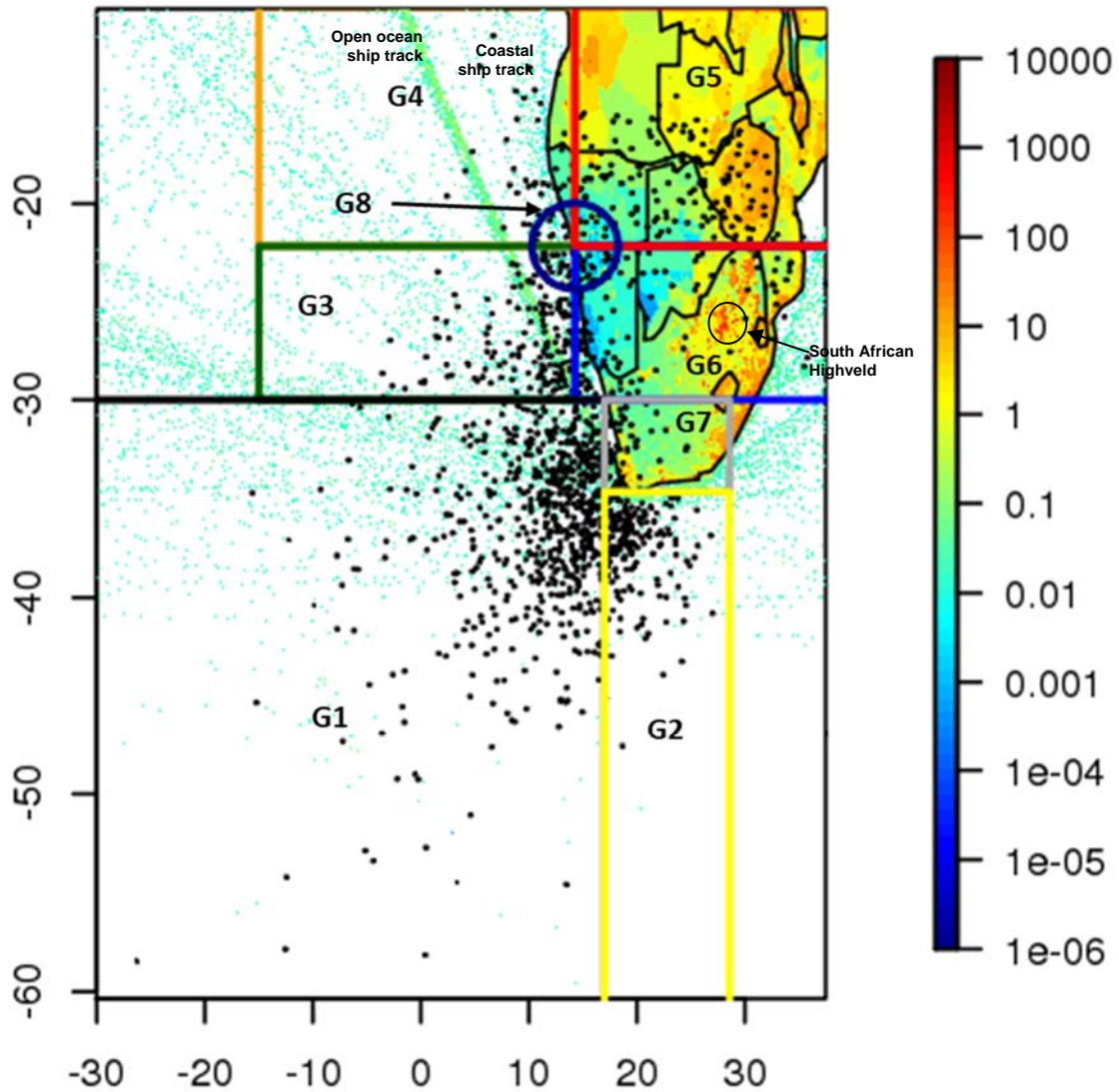
724

725

Figure 4. Fire counts per pixels from MODIS/Aqua provided by the NASA Fire Information for Resources Management System (FIRMS). Colours range from yellow (1 fire count per pixel) to red (+100 fire counts per pixel). The underlying image is the corrected reflectance (true colour) measured by MODIS/Aqua on the first day of each months. Sectors G1 to G8 are indicated over the first image
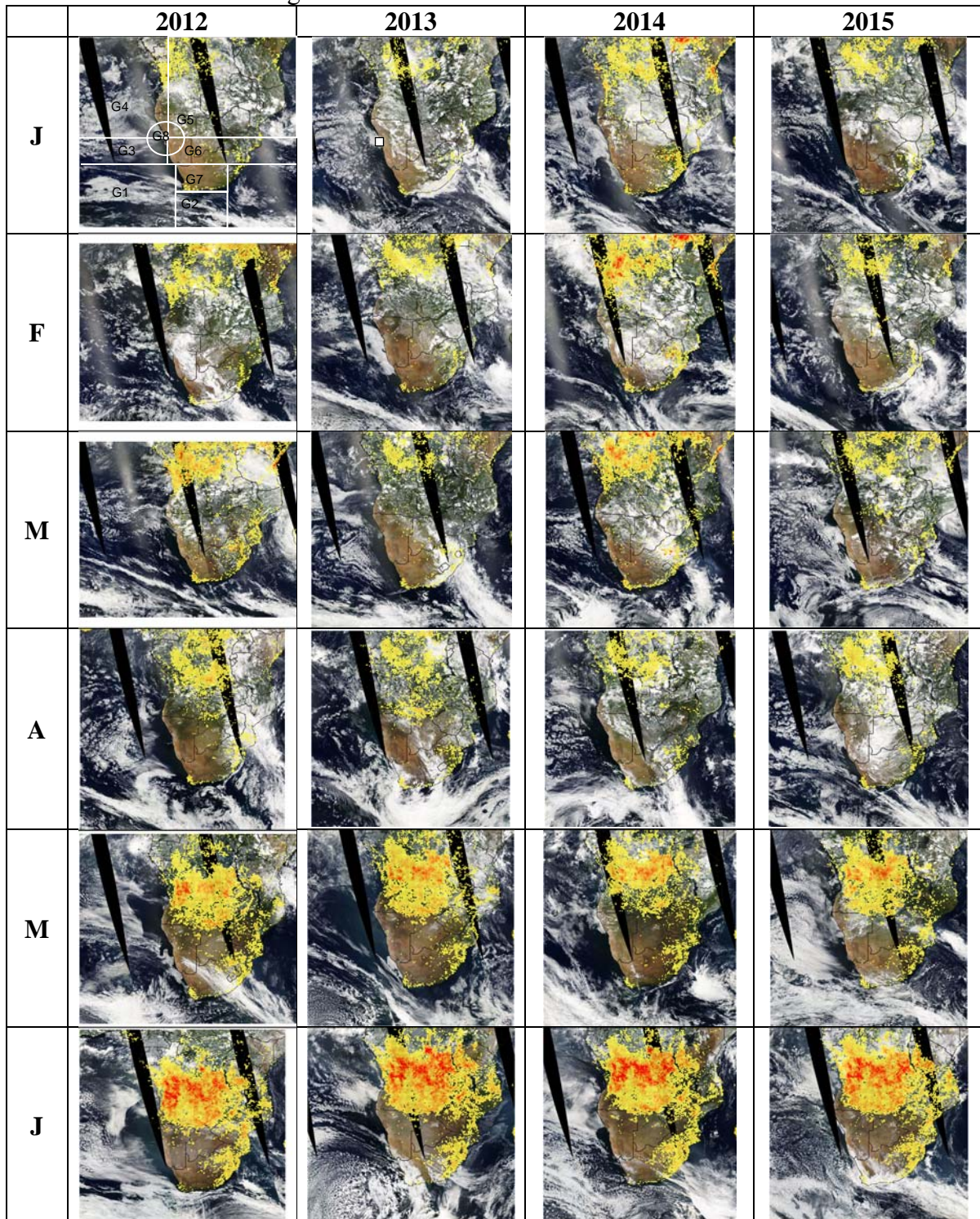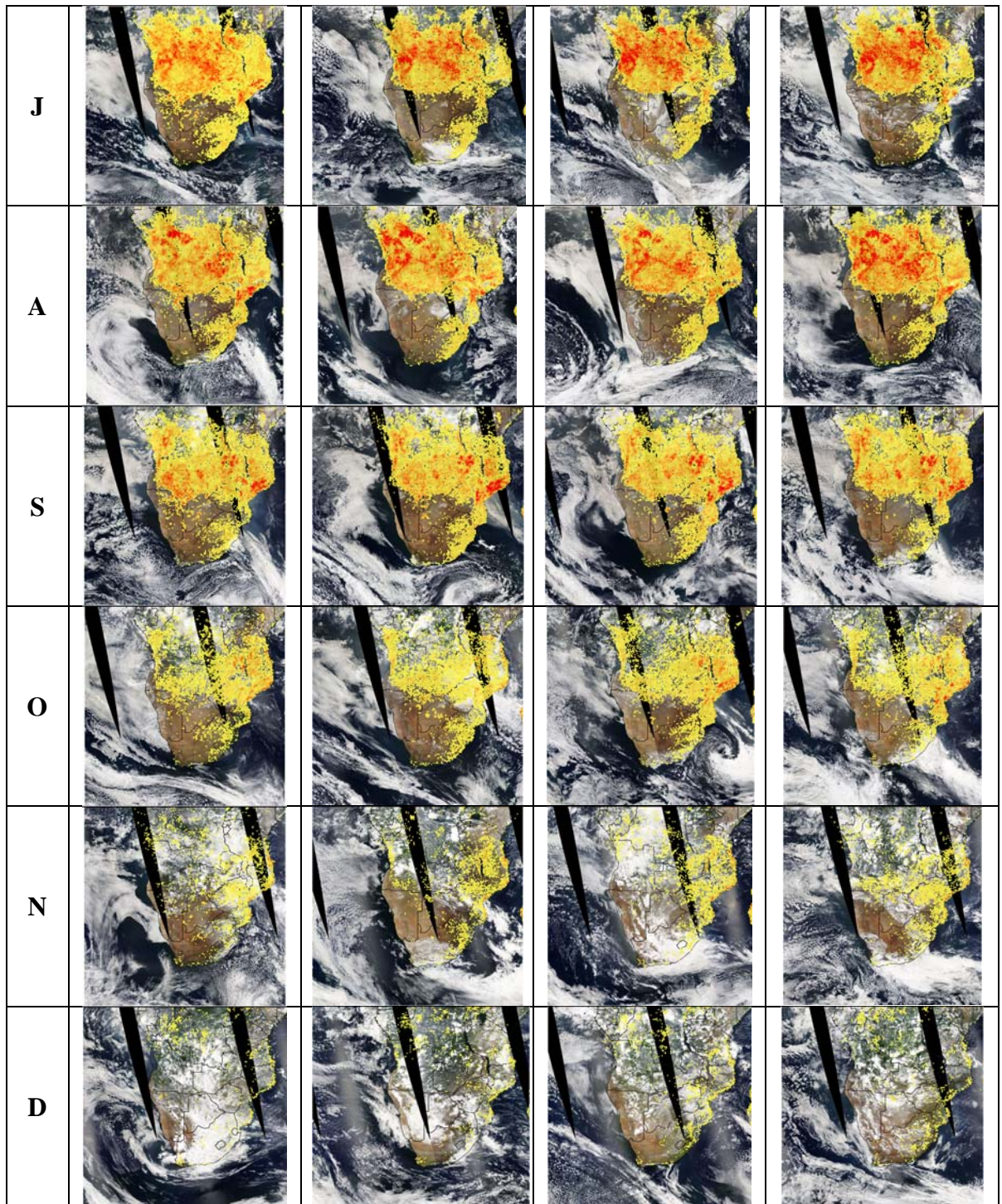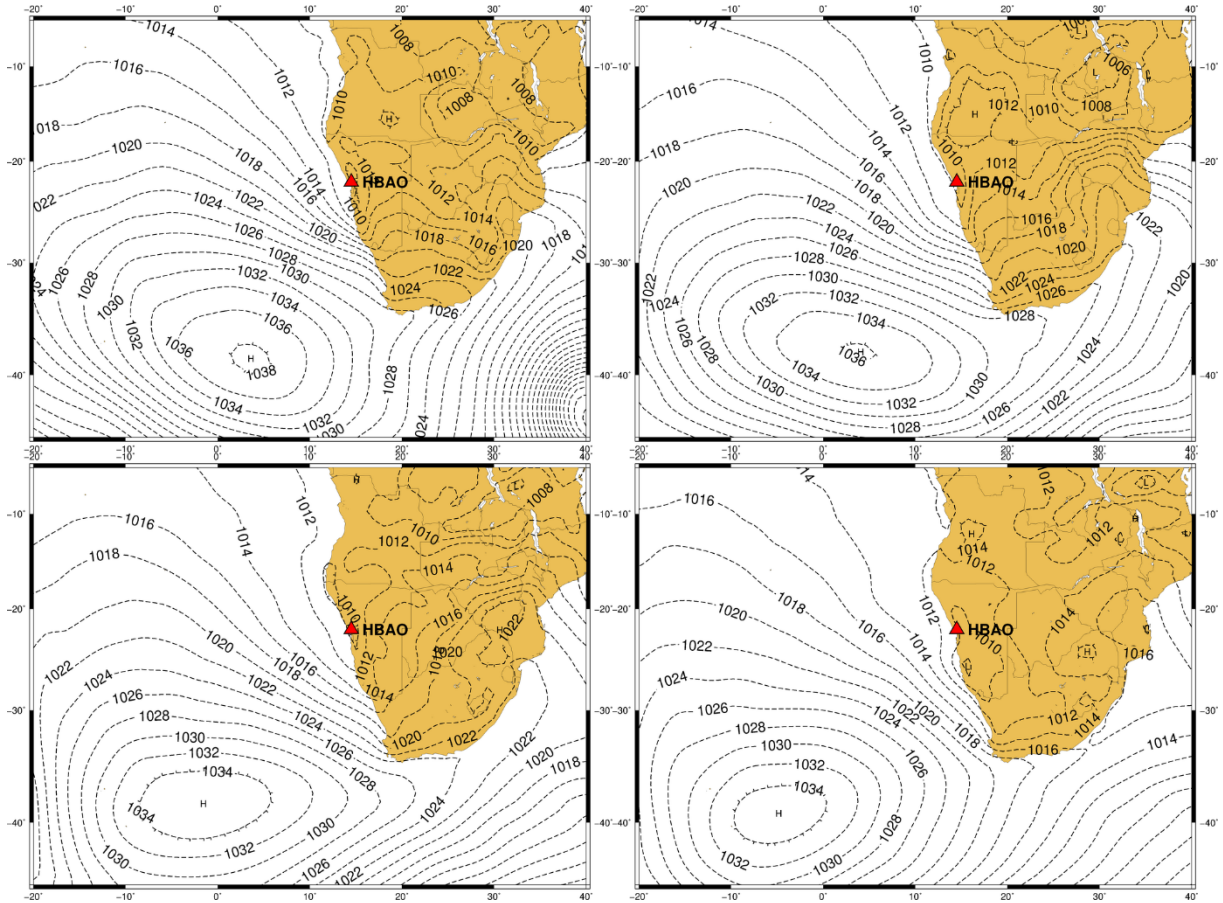
735 **Figure 5**. Seasonal variation in the transport pathways of air masses reaching HBAO between

736 2012 and 2015.
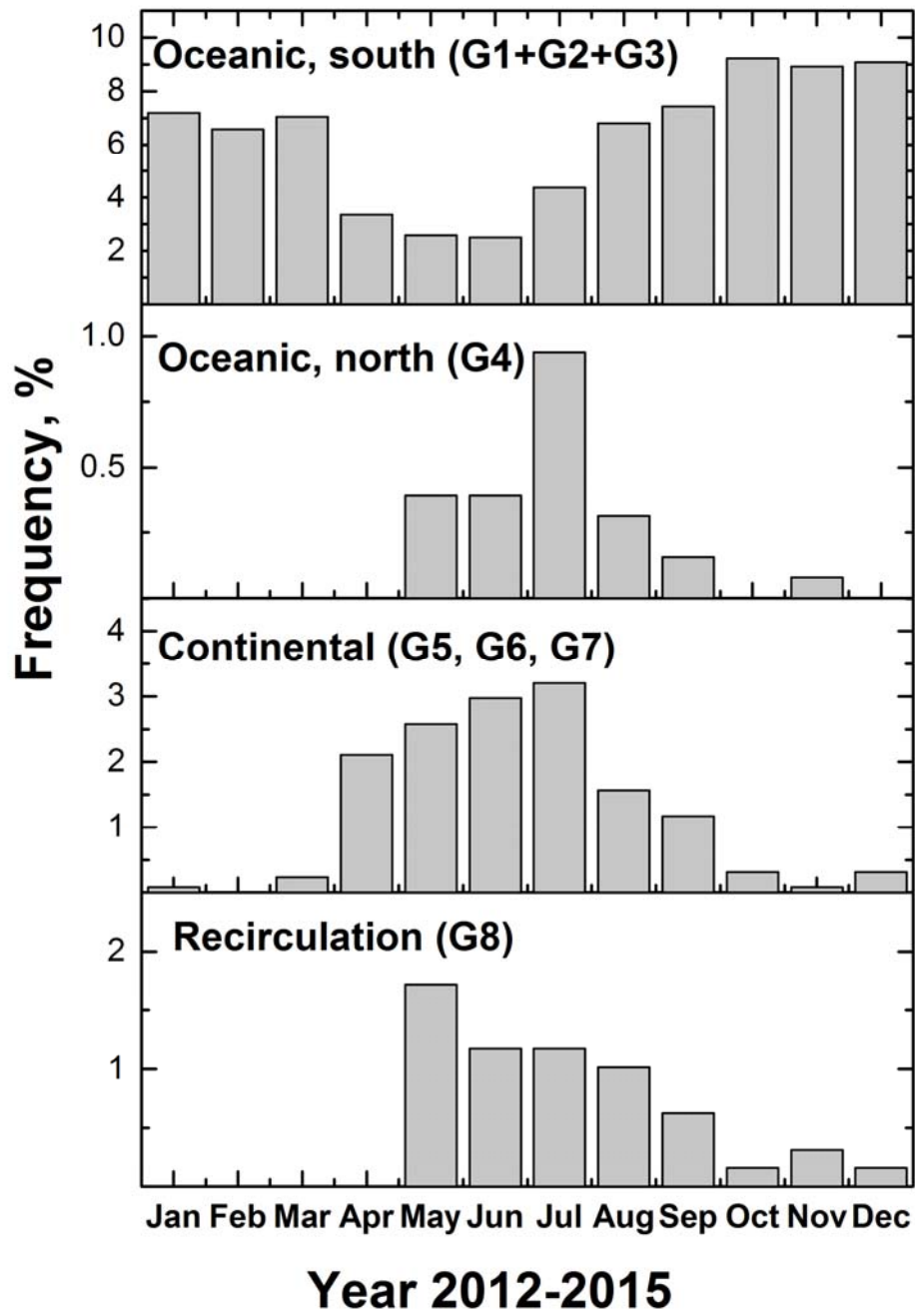
737

738

739 **Figure 6.** Case study of mean sea level pressure over the sub-continent and adjacent South

740 Atlantic Ocean for 16-19 November 2014 illustrating the synoptic circulation that results in the
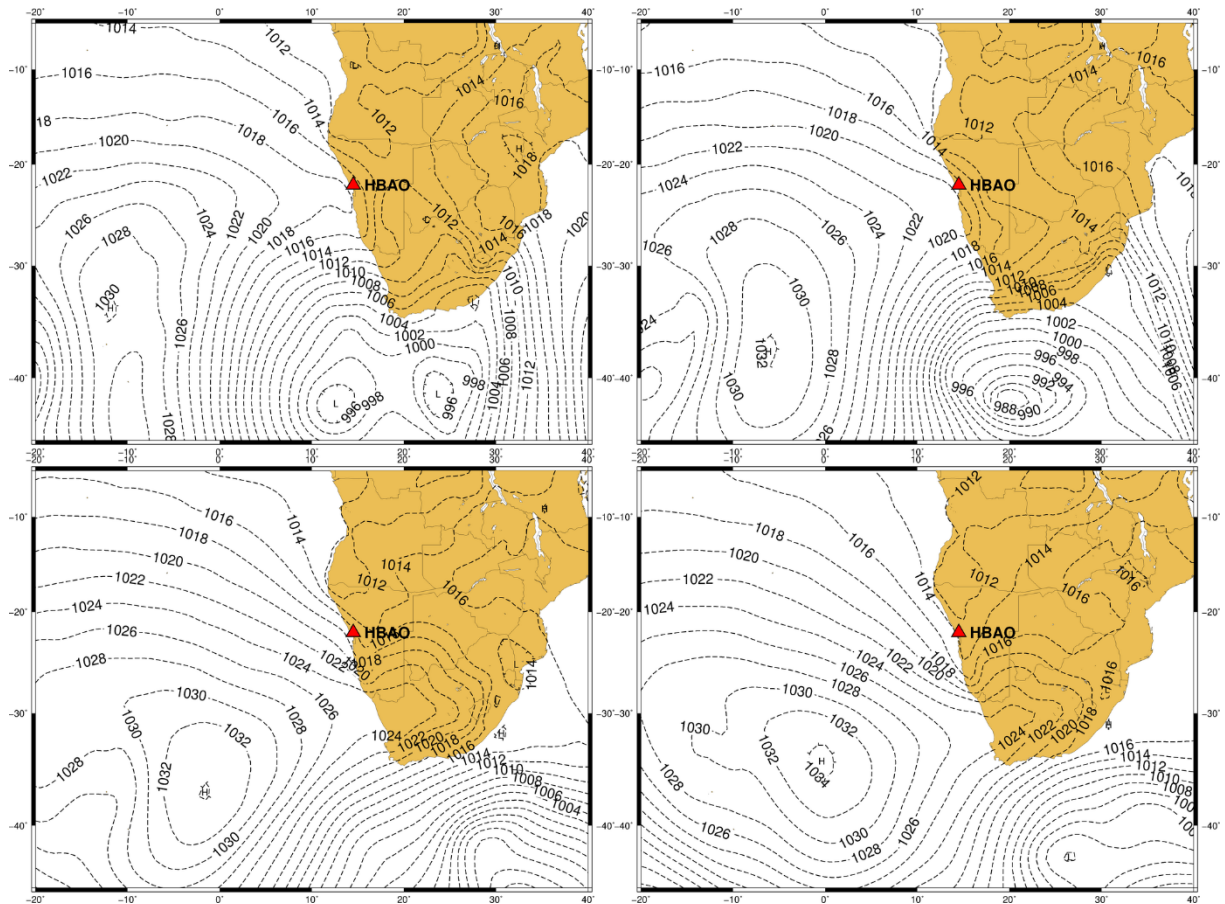
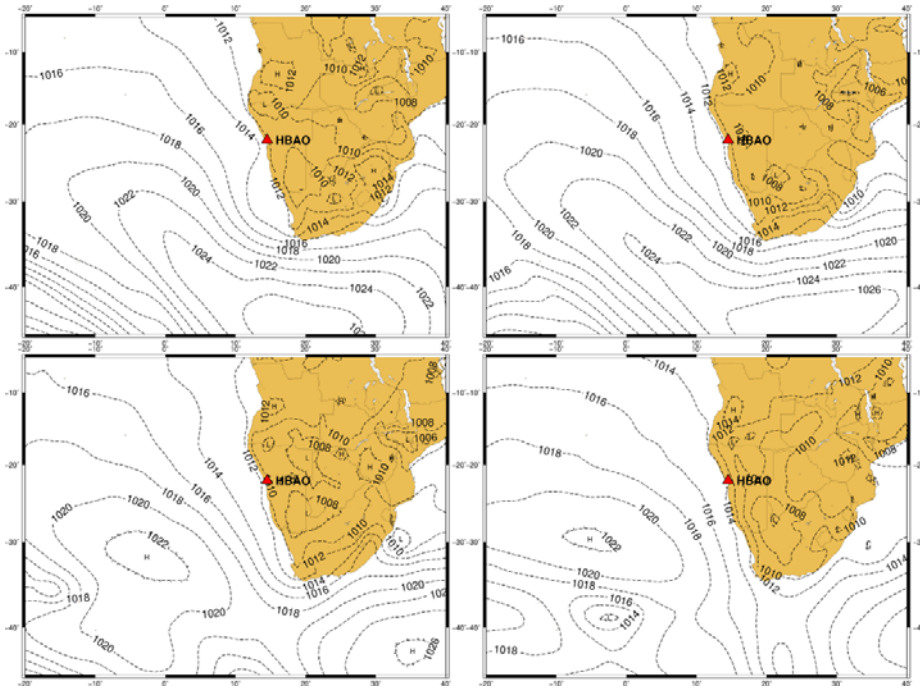741 transport of air masses from sector G1.

742

743

744

745

746 **Figure 7.** Case study of mean sea level pressure over the sub-continent and adjacent South

747 Atlantic Ocean for 1-4 June 3013 illustrating the synoptic circulation that results in the transport
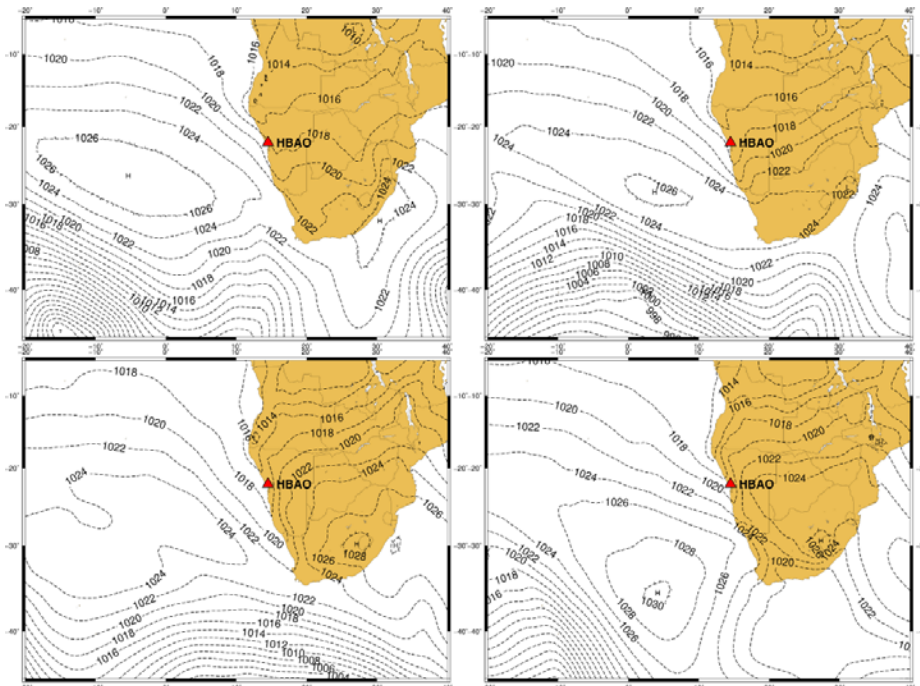
748 of air masses from sector G2.

749

750

751 **Figure 8**. Case study of mean sea level pressure over the sub-continent and adjacent south

752 Atlantic ocean for A) summer (10-13 December 2013) and B) winter (6-10 July 2013)

753 illustrating the synoptic circulation that results in the transport of air masses from sector G5-
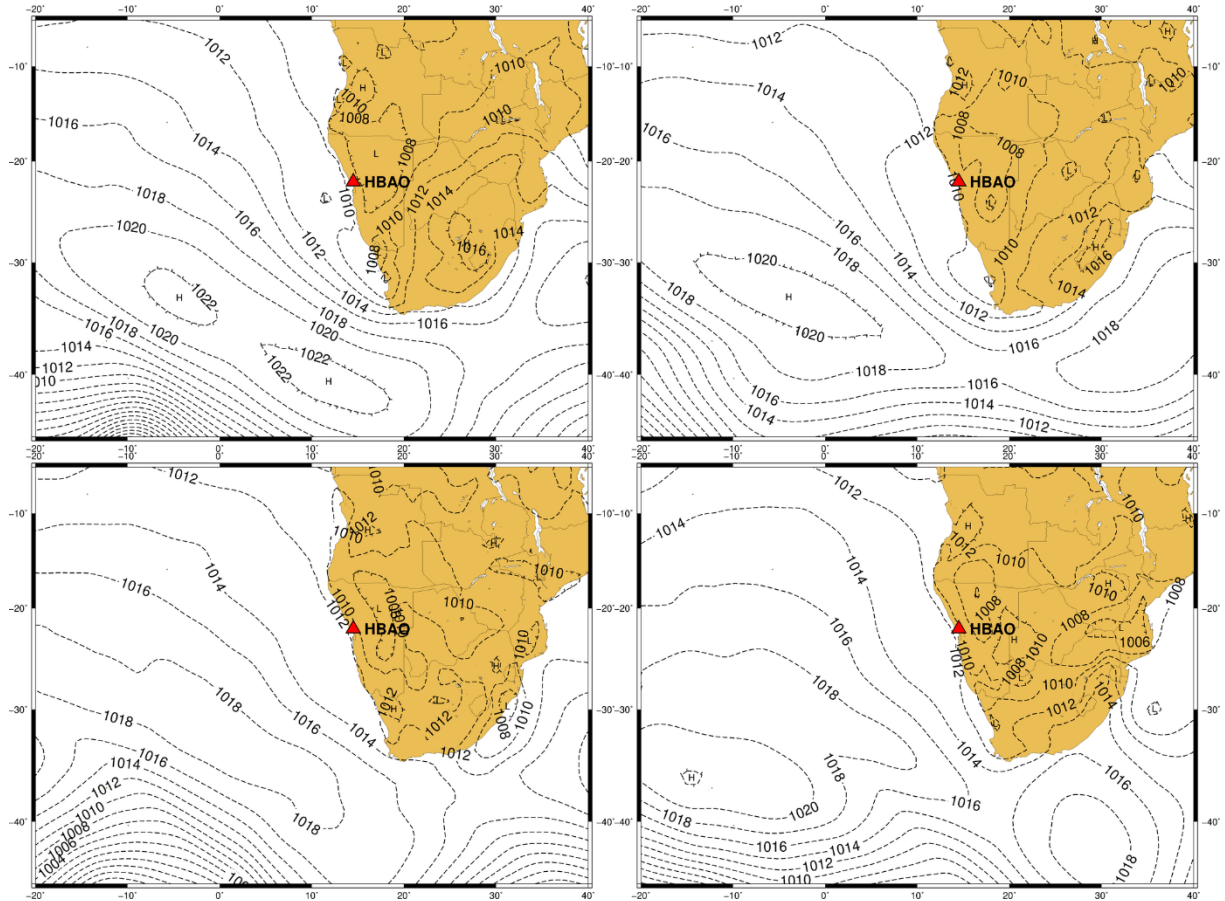
754 G7.

755 A

756

757 B

758

759   **Figure 9**. Case study of mean sea level pressure over the sub-continent and adjacent South

760   Atlantic Ocean for 13-16 December 2012 illustrating the synoptic circulation that results in the

761   transport of air masses from sector G8.

762

763

764

765   **Figure 10**. Contribution of air mass sectors to the eBC concentrations at HBAO from (a) our

766   measurements and (b) MERRA-2 reanalysis.

767

768

769